Enhancing Distorted Metal Organic Framework Derived ZnO as Anode Material for Lithium Storage by the Addition of Ag_2S Quantum Dots

Weixin Song[a], Rowena Brugge[a], Ioannis G. Theodorou[a], Alvin Lukai Lim[b], Yuchen Yang[c], Tingting Zhao[c], Clare H. Burgess[a], Ian D. Johnson[c], Ainara Aguadero[a], Paul R. Shearing[b], Dan J.L. Brett[b], Fang Xie[a], D. Jason Riley[a]*

[a] Department of Materials, Imperial College London, London SW7 2AZ UK. Centre for Nanotechnology, London SW7 2AZ, UK.

[b] Department of Chemical Engineering, University College London, London WC1 E6BT UK.

[c] Department of Chemistry, University College London, London WC1 E6BT UK.

KEYWORDS: Distorted MOFs; ZnO; ZnS; Sulfidation; Lithium storage

---

ABSTRACT: The lithium storage properties of the distorted metal-organic framework (MOF) derived nanosized ZnO@C are significantly improved by the introduction of Ag_2S quantum dots (QDs) during the processing of the material. In the thermal treatment, the Ag_2S QDs react to produce Ag nanoparticles and ZnS. The metal nanoparticles act to shorten electron pathways and improve the connectivity of the matrix and the partial sulfidation of the ZnO surface improves the cycling stability of the material. The electrochemical properties of ZnO@C, Ag_2S QDs treated ZnO@C and the amorphous carbon in ZnO@C have been compared. The small weight ratio of Ag_2S QDs to ZnO@C at 1:180 shows the best performance in lithium storage. The exhibited specific capacities are improved and retained remarkably in the cycling at high current rates. At low current densities (200 mA g^{-1}) treatment of ZnO@C with Ag_2S QDs results in a 38% increase in the specific capacity.

Introduction

Materials for lithium ion batteries must offer high capacity, widespread availability, be environmental benignity, exhibit good conductivity, and excellent stability. Whilst many metal oxides are able to meet the first three of these criteria, they are not employed in devices owing to their limited conductivity and poor stability[1]. The instability of many metal oxide based Li-battery anodes stems from the large volume changes during lithiation-delithiation; for example, bulk ZnO shows a volume change of 228% during charging and discharging. Preparing nanosized metal oxides of well-defined architecture has been demonstrated as a means to mitigate the problem of large volume changes and reduce the distance ions must diffuse, i.e., minimize the resistance. The pyrolysis of Metal Organic Frameworks (MOFs), porous crystalline solids composed of transition metal centers/clusters in coordination with functional organic ligands, offers a facile route to metal oxide-carbon nanocomposites with defined microstructure[2-4]. MOF-5, also called IRMOF-1, has been carbonized in a nitrogen atmosphere at 550 ^{o}C to obtain hierarchically porous carbon-coated ZnO quantum dots (QDs)[5]. The resultant ZnO QDs, with mean particle size of 3 nm, show uniform dispersion without agglomeration in the carbon matrix and the ZnO QDs@porous carbon delivers promising storage performance in lithium-ion batteries. However, the so-called QDs ZnO should be highly dependant on the quality of the MOFs and pyrolysis method affecting the crystal size easily, especially for the MOFs with distorted metal oxide clusters which is common for MOF-5[6-11]. Xie[12] *et al.* and Wang[13] *et al.* have demonstrated that introducing metal nanoparticles into a zinc oxide-carbon composite improves electron transport. It is reported that the as formed materials showed enhanced reversible capacitance, improved rate performance and greater stability.

Zinc sulfide has a slightly lower theoretical capacity to that of zinc oxide but the percentage volume change on lithiation-delithiation of the former material is reduced. This suggests lithium battery anodes incorporating zinc sulfide will be more stable than zinc oxide anodes. Fu[14] *et al.* prepared a ZnS-carbon composite by reacting carbonized ZnO from pyrolysis of MOF-5 with thioacetamide in an autoclave for 24 h. It was demonstrated that the resultant precipitate was an excellent anode material in a Li-ion battery. Sulfidation of ZnO has also been employed to prepare materials for supercapacitors[15]. It was demonstrated that partial sulfidation of ZnO yielded a beneficial ZnO@ZnS material that possessed high capacity and excellent stability. The interface effect in the nanocrystals of the heterostructure induces electric field resulting in low ion-diffusion resistance and facile electron transfer[16-17].

The aim of this work is to enhance the performance of a carbon-metal oxide network formed upon pyrolysis of the distroted MOFs by the introduction of metal nanoparticles into the matrix, to enhance electron transport and connectivity, and the partial sulfidation of the surface of the oxide, to improve stability, in a simple one-step reaction, see Scheme 1. MOF-5 was synthesized by refluxing terephthalic acid (H_2BDC) and $Zn(NO_3)_2 \cdot 6H_2O$ in N,N-dmethylacetamide (DMA). The decomposition of MOF-5 in an argon atmosphere at 550 °C was performed to produce a nanosized ZnO-carbon composite (ZnO@C550). The resultant material was suspended in a glucose solution containing silver sulfide (Ag_2S) quantum dots (SSQD) and subject to a hydrothermal reaction. Pyrolysis of the resultant material was performed at 550 °C to yield a ZnO-ZnS-Ag-carbon composite. The performance of the ZnO-ZnS-Ag-carbon composite as an anode in a lithium ion battery was compared to the parent ZnO@C550, a carbon anode (C550) prepared by treating ZnO@C550 in strong base and a ZnO@C550 sample processed in a glucose solution in the absence of Ag_2S particles (ZnO@CC). It was demonstrated that the decomposition of the Ag_2S QDs within the ZnO-carbon matrix resulted in a material with enhanced capacity and excellent cyclability.

Materials and Methods

Synthesis of MOF-5: 0.95 g terephthalic acid and 5.03 g $Zn(NO_3)_2 \cdot 6H_2O$ were dissolved in 80 mL N,N-dimethylacetamide (DMA) in a 100 mL flask at room temperature. The solution was then continuously stirred at 600 rpm and refluxed at 120 °C for 17 h, heating rate 5 °C min^{-1}. The precipitate obtained was collected after the solution had cooled down and was washed with DMA three times before drying under vacuum overnight at 80 °C.

Synthesis of ZnO@C: The prepared MOF-5 was sintered at 550 °C and 700 °C in an Ar atmosphere, heating was performed at a rate of 8 °C min^{-1} followed by direct cooling. The samples obtained were denoted ZnO@C550 and ZnO@C700, respectively.

Synthesis of C550: 240 mg of as-prepared ZnO@C550 was mixed with 30 mL 3 mol L^{-1} KOH solution and stirred overnight. The precipitate was centrifuged and washed with water several times to remove K^+ ions before drying in an oven at 80 °C. The powder was black and denoted C550.

Synthesis of ZnO@CC: 180 mg ZnO@C550 was added into 20 mL 0.1 mol L^{-1} solution of glucose and stirred for 30 min before transfer to the 120 mL autoclave. The autoclave was put into the oven and heated at a rate of 5 °C min^{-1} to 180 °C, left for 2 h and then cooled down to room temperature. The solution was then filtered and washed with ethanol and water several times before drying in vacuum at 80 °C.

Synthesis of Ag_2S quantum dots (SSQD): Silver sulfide (Ag_2S) quantum dots (SSQD) were synthesized *via* thermal-decomposition of silver diethyldithiocarbamate, Ag(DDTC) as described in the literature[18]. Briefly, 0.1 mmol of Ag(DDTC) was added to 10 g of 1-dodecanethiol (DT) in a 100 mL three-necked flask at room temperature. Oxygen was removed from the slurry with vigorous magnetic stirring under vacuum for 5 min. The reaction flask was refilled with Ar and the reaction temperature was raised to 130 °C at a rate of 10 °C min^{-1} and retained at this temperature for 1 min to allow the growth of 2.7 nm SSQDs. The solution was cooled to room temperature under ambient atmosphere and 50 mL of ethanol was subsequently poured into the solution. Ag_2S QDs were collected by centrifugation at 16,000 g for 30 minutes. In order to render Ag_2S QDs hydrophilic with a carboxylic acid group capping, ligand exchange of DT with dihydrolipoic acid (DHLA) was performed.[19] A mixture of as-prepared Ag_2S QDs (10 mg), cyclohexane (15 mL), ethanol (15 mL), and DHLA (100 g) was stirred at room temperature for 48 h. The hydrophilic Ag_2S QDs were collected by centrifugation at 16,000 g for 1 h, washed with deionized water twice, redispersed in deionized water and stored at 4 °C in the dark.

Synthesis of SSQD inlayed ZnO/C: 200 µL of as-prepared SSQD solution (5 mg mL^{-1}) was mixed with 20 mL 0.1 mol L^{-1} solution of glucose by stirring. Then 180 mg ZnO@C550 was added and stirred for 30 min before transfer to the 120 mL autoclave. The autoclave was put into the oven and heated at a rate of 5 °C min^{-1} to 180 °C, left for 2 h and then cooled down to room temperature. The solution was then filtered and washed with ethanol and water several times before drying in vacuum at 80 °C. The powder obtained was heated in Ar at a rate of 2 °C min^{-1} to a temperature of 550°C and calcined for 5 h to transfer SSQDs into the ZnO@C composite, the final material being denoted as ZnO@CC/SSQD$_m$. Similarly, when 600 µL SSQD solution was used with 180 mg ZnO/C550 with the same method, the product was labeled ZnO@CC/SSQD$_{3m}$.

Material Characterization: The crystallographic structure of the as-prepared materials was studied by X-ray powder diffraction (XRD) using a Bruker D8 diffractometer with monochromatic Cu Kα radiation (λ = 1.5406 Å), and the diffraction data was recorded in the 2θ range of 10–80 °. Scanning electron microscopy (SEM) images were recorded on a LEO Gemini 1525 FEG with the electron energy of 5 kV. Electron Dispersive X-Ray Spectroscopy (EDS) was recorded on LEO Gemini 1525 FEG microscopy. Transmission electron microscopy (TEM) images, selected area electron diffraction (SAED), scanning transmission electron microscopy (STEM) were carried out on a JEM 2100F. X-ray photoelectron spectroscopy (XPS) was measured on a Thermo Scientific K-Alpha instrument. Raman spectroscopy was performed using a RenishawinVia with 20× objective and 514 nm laser as excitation source. The thermogravimetric analysis/differential scanning calorimetry (TGA/DSC) of the samples was carried out on a Diamond TG thermo-analyzer.

Electrochemical Tests: The as-prepared material was mixed with acetylene black and binder (sodium carboxymethyl cellulose, CMC) in a weight ratio of 8:1:1 by using distilled water as the solvent and a copper foil as the current collector, followed by drying in vacuum at 100 ^{o}C for 24 h. The R2016 coin cell was assembled in an argon-filled glove box using metallic lithium as the cathode and Celgard 2500 membrane as the separator. The electrolyte was 1 M $LiPF_6$ dissolved in a mixture of ethylene carbonate (EC), dimethyl carbonate (DMC) (v/v, 1/1). Cyclic voltammetry (CV) and galvanostatic charge/discharge cycling tests were carried out in a set voltage range using an Autolab workstation (GPES software) and a 580 Bycycle battery test system, respectively. Electrochemical impedance spectroscopy (EIS) was studied using a Solartron Analytical 1260 FRA and a Solartron 1286 potentiostat, an amplitude of 5 mV in the frequency range from 1000 Hz to 10 mHz was applied. All electrochemical tests were carried out at room temperature.

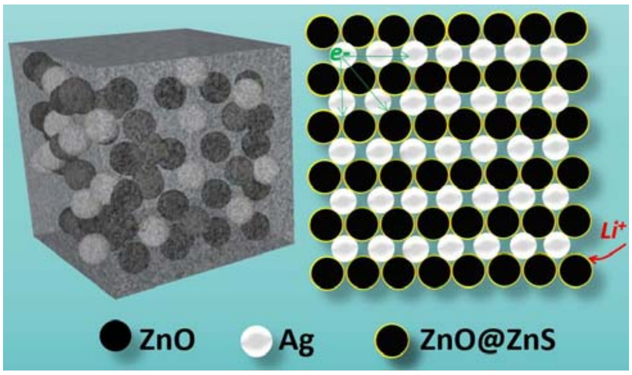

Scheme 1 Ag_2S QDs decompose in the pyrolysis of cubic ZnO@C (left) to produce ZnS layer on the surface of ZnO@C matrix and silver nanoparticles conductor (right).

Results and Discussion

The as-synthesized MOF-5 has a structural formula of $Zn_4O(BDC)_3$ that reticulates cubes in three dimensions to form a rigid and porous structure, as depicted in the inset of Figure 1a (also see Figure S1)[20-21]. The central cluster of MOF-5 is zinc oxide, resulting from the combination of Zn^{2+} and carboxylic acid, and the Zn-O-C motifs are formed and linked with benzene struts[20-21]. Figure 2a indicates that at a 2θ value greater than 30° the XRD pattern of the as-prepared MOF-5 displays peaks that match those of zincite. At lower angles, the positions of the peaks are in good agreement with those calculated for MOF-5[6-8]. However, the measured intensities of the XRD peaks, especially at low-angles, are different from those calculated and published[11, 22]. It has been reported that this discrepancy may result from species, e.g. $Zn(OH)_2$, in the pores that can reduce the intensity of the diffraction at 6.9° and split the peak, owing to a symmetry distortion from cubic to trigonal, at 9.7°. On pyrolysis of the as-formed MOF at 550 °C and 700 °C in an Ar atmosphere, denoted ZnO@C550 and ZnO@C700 respectively, composites containing zincite (ZnO) are obtained, as evidenced by the diffraction pattern in Figure 1b and Figure S2. The crystal size of ZnO in ZnO/C550, calculated by application of the Scherrer equation on the (103) peak, is 25 nm resulting from the distorted metal cluster in the MOFs. When ZnO/C550 was placed in a glucose solution, hydrothermally treated and the recovered solid calcined at 550 °C, the XRD pattern of the resultant solid, ZnO@CC, indicated that the zincite was maintained throughout the processing (Figure S2). Zincite is also observed in the XRD patterns, Figure 1b, obtained when 2.7 nm SSQDs (Figure S3) are added to the glucose solution at Zn to Ag ratios in mass of 180:1 and 60:1 prior to processing, samples termed $ZnO@CC/SSQD_m$ and $ZnO@CC/SSQD_{3m}$, respectively. The XRD pattern of the sample infused with the greater concentration of SSQDs, $ZnO@CC/SSQD_{3m}$, also shows weak features at 2θ angles of 38.1 ^{o} and 44.2 ^{o} consistent with the (111) peaks and (200) peaks of silver metal, indicating the silver sulfide particles undergo thermal decomposition when heated to give silver nanoparticles in the resultant matrix.

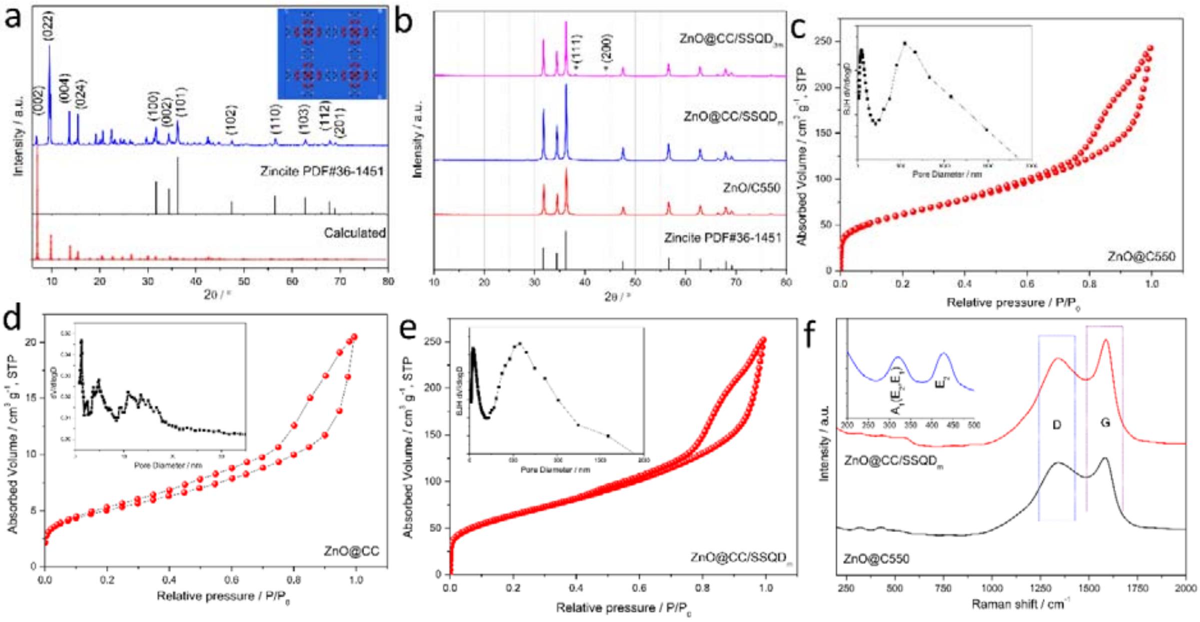

Figure 1 (a) XRD patterns of the as-prepared MOF-5. References are XRD patterns from zincite and the calculated MOF-5 crystallite. The inset is the schematic structure of MOF-5; the red spheres are O atoms, white spheres are H atoms, black spheres are C atoms and blue spheres are Zn atoms. (b) XRD patterns of ZnO@C550, ZnO@CC/SSQD$_m$ and ZnO@CC/SSQD$_{3m}$. N_2 absorption/desorption curve of: (c) ZnO@C550, (d) ZnO@CC and (e) ZnO@CC/SSQD$_m$. The inset is the corresponding pore size distribution curve. (f) Raman spectra of ZnO@C550 and ZnO@CC/SSQD$_m$.

N_2 absorption/desorption isotherms of ZnO@C550, ZnO@CC and ZnO@CC/SSQD$_m$ are shown in Figure 1c-e, which are typical type IV curves. The Brunauer–Emmett–Teller (BET) theory was used to deduce the surface area of all the samples, the pore size distributions of ZnO@C550 and ZnO@CC/SSQD$_m$ were determined using the Barret-Joyner-Halenda (BJH) method on account of their mixed macroporosity and mesoporosity, Density Functional Theory (DFT) was employed to find the pore size distribution of the mesoporous ZnO@CC sample. ZnO@C550 has a BET surface area of 222 m^2 g^{-1}, with pore sizes distributed around 49 and 545 nm and a pore volume of 0.352 m^3 g^{-1}. ZnO@CC has a BET surface area of 252 m^2 g^{-1}, a pore size below 20 nm and a pore volume of 0.387 m^3 g^{-1}. ZnO@CC/SSQD$_m$ shows 231 m^2 g^{-1} with pore sizes around 41 and 576 nm and a pore volume of 0.366 m^3 g^{-1}. The enlarged surface area and pore volume of ZnO@CC and ZnO@CC/SSQD$_m$ indicates that the penetrated glucose in the pores larger than micro size, has decomposed in hydrothermal and calcination treatment to become amorphous carbon which contributes more pore area and volume[23]. The total carbon contents of ZnO@C550, ZnO@CC and ZnO@CC/SSQD$_m$ are 20%, 17.4% and 14.3%, respectively, see Figure S4. Figure 1f displays the Raman spectra of ZnO@C550 and ZnO@CC/SSQD$_m$. ZnO has optical phonons represented as A_1, E_1, $2E_2$ and $2B_1$ amongst which the A_1 and E_1 modes are polar modes active for both Raman and Infrared, the E_2 mode is nonpolar only active for Raman and the B_1 mode is a silent mode[24]. A_1 and E_1 modes split into longitudinal (LO) and transverse (TO) components, and the E_2 mode comprises low-frequency phonons, $E_2(L)$, and high-frequency phonons, $E_2(H)$. The bands around 435 and 327 cm^{-1} (inset of Figure 1f) are due to the $E_2(H)$ mode and multi-phonon scattering consisting of predominant A_1 and smaller E_2 and E_1 symmetry[24-25]. The bands at 1340 and 1589 cm^{-1} are typical D and G modes of carbon materials, and the intensity ratio of I_D/I_G is indicative of the fraction of graphite structure[23]. The I_D/I_G ratios of ZnO@CC/SSQD$_m$ and ZnO@C550 are 0.83 and 0.95 respectively, indicating that the degree of graphitization increases as glucose decomposes in ZnO@C550.

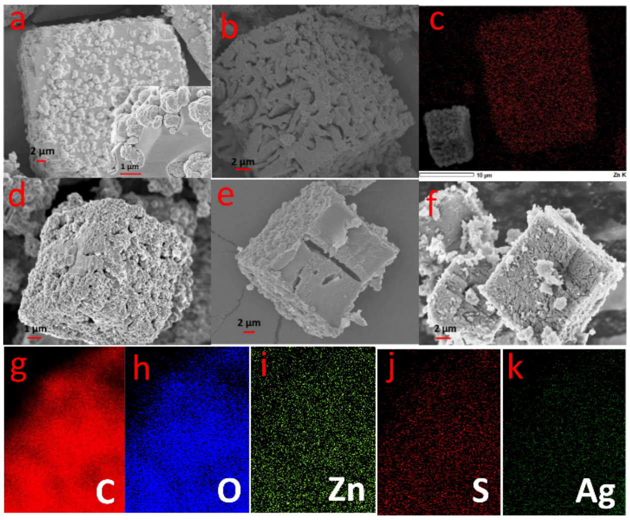

Figure 2 SEM images of (a) Zn-MOF, (b) ZnO@C550, (d) ZnO@CC/SSQD$_m$, (e) ZnO@CC/SSQD$_{3m}$ and (f) C550.

EDS Elemental mapping of (c) ZnO@C550 and (g-k) ZnO@CC/SSQD$_{3m}$.

The scanning electron microscopy (SEM) image of the as-prepared MOF-5 shows a cubic microstructure with a rough surface (Figure 2a). The surface is patterned with spherical solids of approximately 1 μm inlayed into the MOF-5 matrix (inset of Figure 2a). On calcination at 550 °C the resultant ZnO@C550 is transformed into a highly porous composite in which the cubic sized particles of the parent MOF are maintained, see Figure 2b. Elemental mapping indicates that the Zn is dispersed uniformly in the ZnO@C550 composite, Figure 2c. In ZnO@C700, formed at the higher sintering temperature of 700 °C, the cubic structure is destroyed, see Figure S5, and the composite contains smaller sized features. Exposure of ZnO@C550 to glucose solution and glucose solution containing SSQDs followed by hydrothermal processing and calcination at 550 °C does not alter further the microstructure of the composite, Figures 2d and e. The cubic microstructure is again preserved, Figure 2f, when ZnO@C550 is subject to treatment in a strong base to dissolve the ZnO and yield C550, which is composed of amorphous carbon, as indicated by the broad XRD peak at approximately 22°, (see Figure S6)[26]. Elemental mapping of ZnO@CC/SSQD$_{3m}$, Figure 2(g-k), shows Ag agglomerates and a uniform distribution of C, O and Zn. EDX also shows the presence of S in the composite, the nature of the S in the material is discussed below.

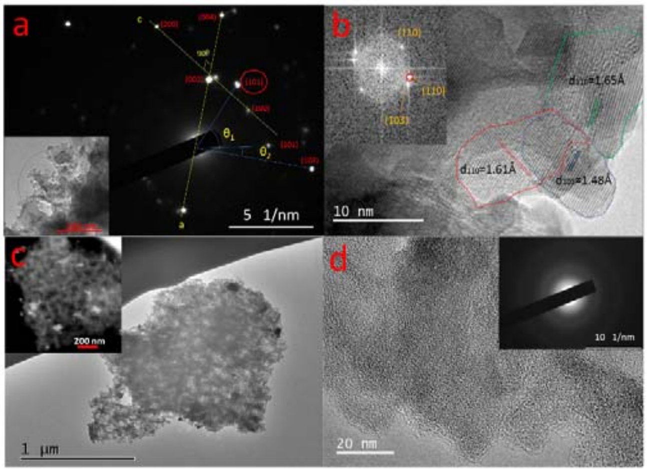

Figure 3 (a) SAED of the circle part from TEM images of ZnO@CC/SSQD$_m$. (b) HRTEM image of ZnO@CC/SSQD$_m$, the inset is the FFT pattern from the mixed area. (c) BF and DF STEM images of ZnO@CC/SSQD$_m$. (d) TEM images of C550 and the corresponding SAED pattern.

ZnO@CC/SSQD$_m$ was subject to intense sonication to destroy the cubic microstructure and yield particles suitable for TEM analysis. Figure 3a shows that ZnO@CC/SSQD$_m$ contains nanosized components and a selective area electron diffraction (SAED) pattern of the sample, is consistent with a material containing ZnO crystals. Two unrelated reciprocal points from (101) planes are observed, pointing to interpenetration of ZnO crystals with random lattice orientations. The axes labelled a and c are at an angle of 90° and the reciprocal points of the (101) and (103) planes from a single zincite crystal have an angle of approximately 30° (see Figure S7). Comparing θ_1 and θ_2, the point circled is formed from the second crystal. The polycrystalline nature of the material is confirmed in the HRTEM image in Figure 3b in which the (103) and (110) lattice planes of ZnO are both observed. The two (110) planes show different orientations, indicating they originate from different ZnO crystal. The Fast Fourier Transform (FFT) image of the lattice mixed area in Figure 3b is displayed in the inset. In reciprocal space the (110) plane is at 40° with respect to the (101) plane when viewed along the [1,-1, -1] direction (Figure S7b) and the stereographic projection, see Figure S7c, indicates that the (110) plane should be at an angle larger than 40° with (103) plane. Therefore, the red circled (110) plane in the inset corresponding to the green dotted plane (d=1.65 Å) in HRTEM is from the second crystal. The bright field (BF) and dark field (DF) scanning transmission electron microscope (STEM) images in Figure 3c illustrate the porous structure of ZnO@CC/SSQD$_m$. That the carbon component is amorphous is confirmed by the TEM images of C550 and the corresponding electron diffraction patterns in Figure 3d.

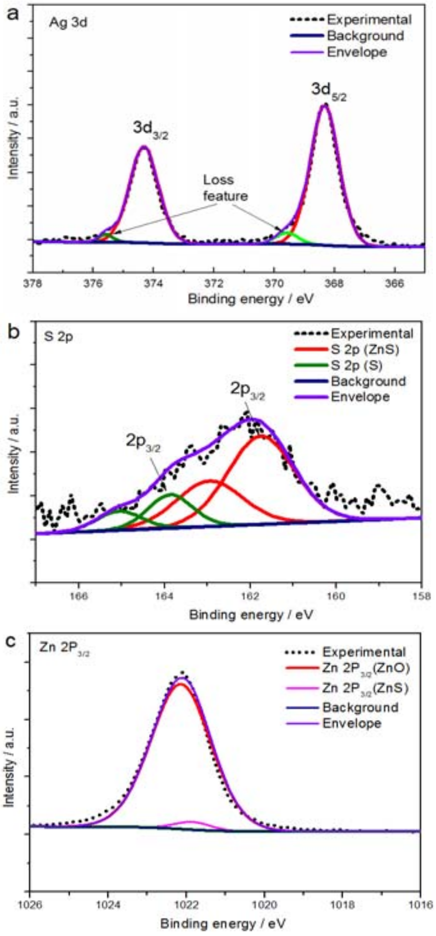

Figure 4 High resolution XPS spectra of (a) Ag 3d, (b) S 2p and (c) Zn 2P$_{3/2}$ of ZnO@CC/SSQD$_m$.

Figure 4 displays the high-resolution XPS spectra of Ag, S and Zn of ZnO@CC/SSQD$_m$. The spectrum of Ag 3d in Figure 4(a) shows characteristics typical of a metal[27]. This spectrum contains two components: one at 368.3 eV for Ag 3d$_{5/2}$ and the other at 374.3 eV for Ag 3d$_{3/2}$, the difference in binding energy of 6 eV results from spin-orbital effects[28]. The orbital spin of silver metal leads to the loss of features at the higher binding energy side of each component. The intensity of the S 2p spectrum, Figure 4(b), is considerably weaker than that for Ag. The S 2p spectrum is consistent with the presence of ZnS and a very small amount of S in the as-prepared composite, with the absence of Ag-S confirming that all the SSQds have been reacted to Ag nanoparticles, in agreement with the Ag 3d XPS deconvolution and XRD analysis. The S 2p$_{3/2}$ of ZnS is located at 161.7 eV and that of S is at 163.8 eV[29]. The spin-orbit of S 2p results in 1.16 eV difference between S 2p$_{3/2}$ and S 2p$_{1/2}$. In agreement, the Zn 2p spectrum, Figure 4(c) displays two 2p$_{3/2}$ components at 1022.1 and 1021.9 eV pointing to Zn-O and Zn-S respectively[29-31]. The spin orbital of Zn 2p results in a pair of 2p$_{3/2}$ and 2p$_{1/2}$ with a difference of 23 eV in binding energy. The atomic ratio of S:Ag:Zn is 0.9:7.6:91.5 through the XPS survey of S 2p$_{3/2}$, Ag 3d$_{5/2}$ and Zn 2p$_{3/2}$, see Figure S8. The small amount of ZnS in the composite, consistent with a sub-monolayer of ZnS on the ZnO surface, explains the absence of ZnS signals in the XRD patterns and the Raman spectra. Figure S9 shows the atom ratio of S:Ag:Zn is 2.9:7:90.1 in ZnO@CC/SSQD$_m$, thus the ratio of ZnS:ZnO increased from 1:90 to 1: 30 when 3-times more SSQDs are added in the synthesis of ZnO@CC/SSQD$_{3m}$. The Ag content is found to be lower than that in ZnO@CC/SSQD$_m$, indicating the Ag particles aggregate during sulfidation reaction, consistent with the EDX mapping.

Electrodes comprising ZnO@C550, ZnO@CC, ZnO@CC/SSQD$_m$ and ZnO@CC/SSQD$_{3m}$ were electrochemically tested in coin cells with lithium metal as the counter electrode material. Cyclic voltammograms (CV) of the samples were obtained between 0.01 and 3.00 V vs. Li$^+$/Li at a scan rate of 0.5 mV s^{-1}, see Figure 5. The smaller areas under the CV curves of ZnO@C550 and ZnO@CC, in comparison to the samples ZnO@CC/SSQD$_m$ and ZnO@CC/SSQD$_{3m}$, indicates a lower capacity for the former. This is confirmed by integration of the CV peak at 0.5 V where a larger capacity is observed when SSQDs are used in the processing (see Table S1). The CV measured at 0.5 mV s^{-1} of ZnO@CC/SSQD$_m$ shows more features that those of ZnO@C550, ZnO@CC and ZnO@CC/SSQD$_{3m}$ at the same scan rate. The additional peaks observed in ZnO@CC/SSQD$_m$ can be observed for all electrodes when lower scan rates are employed, for ZnO@C550 see Figure 5b, for ZnO@CC see Figure S10 and for ZnO@CC/SSQD$_{3m}$ see Figure 6d. The fact that the additional features are retained at higher scan rates for ZnO@CC/SSQD$_m$ electrodes points to an enhanced rate performance for this material. Displayed in Figure 5c, the CV curves of ZnO@CC/SSQD$_m$ have two cathodic peaks at 0.55 V and 0.2 V corresponding to the reduction of ZnO/ZnS to Zn (Reaction 1), and the formation of Zn-Li alloys (Reaction 2) and/or the decomposition of electrolyte[30, 32-33]. The multiple anodic peaks before 1 V result from the multi-step de-alloying reaction among LiZn, Li$_2$Zn$_3$, LiZn$_2$ and Li$_2$Zn$_5$ and the peak at 1.5 V is due to the decomposition of Li$_2$O.

$$\boldsymbol{ZnO/ZnS + Li^+ + 2e^- \leftrightarrow Zn + Li_2O/Li_xS}$$

(Reaction 1)

$$\boldsymbol{Zn + Li^+ + e^- \leftrightarrow \left(Li_2Zn_5 \leftrightarrow LiZn_2 \leftrightarrow Li_2Zn_3\right) \leftrightarrow LiZn}$$

(Reaction 2)

CV curves at different scan rates are shown in Figure 5d-f for ZnO@C550, ZnO@CC/SSQD$_m$ and ZnO@CC/SSQD$_{3m}$. For ZnO@C550 the cathodic peak is extremely depressed at high rates and the anodic peak II moves to higher potential with increased scan rate. In contrast, for ZnO@CC/QQSD$_m$ the potential of the CV peaks is stable and for ZnO@CC/SSQD$_{3m}$ peak II downshifts with increasing scan rate. The upshift of the anodic peak with scan rate for ZnO@C550 points to high internal resistance in the system. SSQDs incorporation decreases the resistance, leading to lower distortion of the CV peaks for the ZnO@CC/QQSD$_m$ and ZnO@CC/SSQD$_{3m}$ systems. In cyclic voltammetry the peak current (i_p) and the scan rate (v) are related by the expression i_p=av^b, where b, the slope of the lg(v)-lg(i_p) plot, has a value of 0.5 for a diffusion-controlled process and unity when charge transfer is surface-controlled. Figure S11 shows the relationship between lg(v) and lg(i_p) of peak I and peak II from ZnO@C550 and ZnO@CC/SSQD$_{3m}$, respectively. The b values from peak I and peak II of ZnO@C550 are 0.69 and 0.76 and for ZnO@CC/SSQD$_{3m}$ are 0.98 and 0.8 at a scan rate above 0.2 mV s^{-1}. The switch to surface control of the electrochemical reaction in ZnO@CC/SSQD$_{3m}$ at high scan rates indicates a more facile injection of Li$^+$ into the ZnS coated material at high current densities[34]. The Li$^+$ ion-diffusion capability is evaluated by the appeerent diffusion coefficient. The linear relationship between the anodic peak current (i_p) and square root of scan rates resulting from the CV curves of ZnO@C550 and ZnO@CC/SSQD$_{3m}$ is depicted in Figure S12. Thus the ion diffusion coefficients are calculated using the Randle-Sevcik equation[35-36]. It is found that the coefficients are 3.6×10^{-11} and 1.7×10^{-11} cm^2 s^{-1} for anodic peaks I and II respectively of ZnO@C550 and increase to 9.9×10^{-10} and 4.7×10^{-10} cm^2 s^{-1} for ZnO@CC/SSQD$_{3m}$, demonstrating the facile lithium diffusion in the compound after sulfidation.

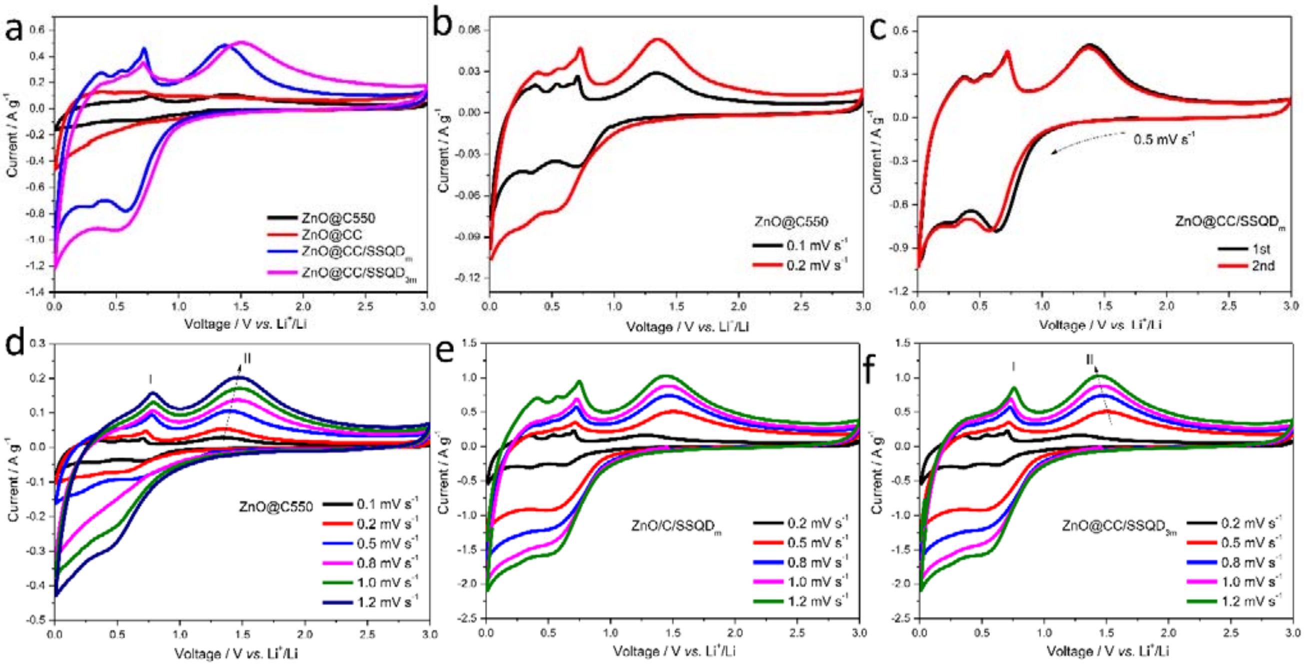

Figure 5 Cyclic voltammetry of the as-prepared materials. (a) Scan rate is 0.5 mV s^{-1} for ZnO@C550, ZnO@CC, ZnO@CC/SSQD$_m$ and ZnO@CC/SSQD$_{3m}$. (b) ZnO@C550 cycled at 0.1 and 0.2 mV s^{-1}. (c) First two cycles of ZnO@CC/SSQD$_m$ at 0.5 mV s^{-1}. Cycles at different scan rates of (d) ZnO@C550, (e) ZnO@CC/QQSD$_m$ and (f) ZnO@CC/SSQD$_{3m}$.

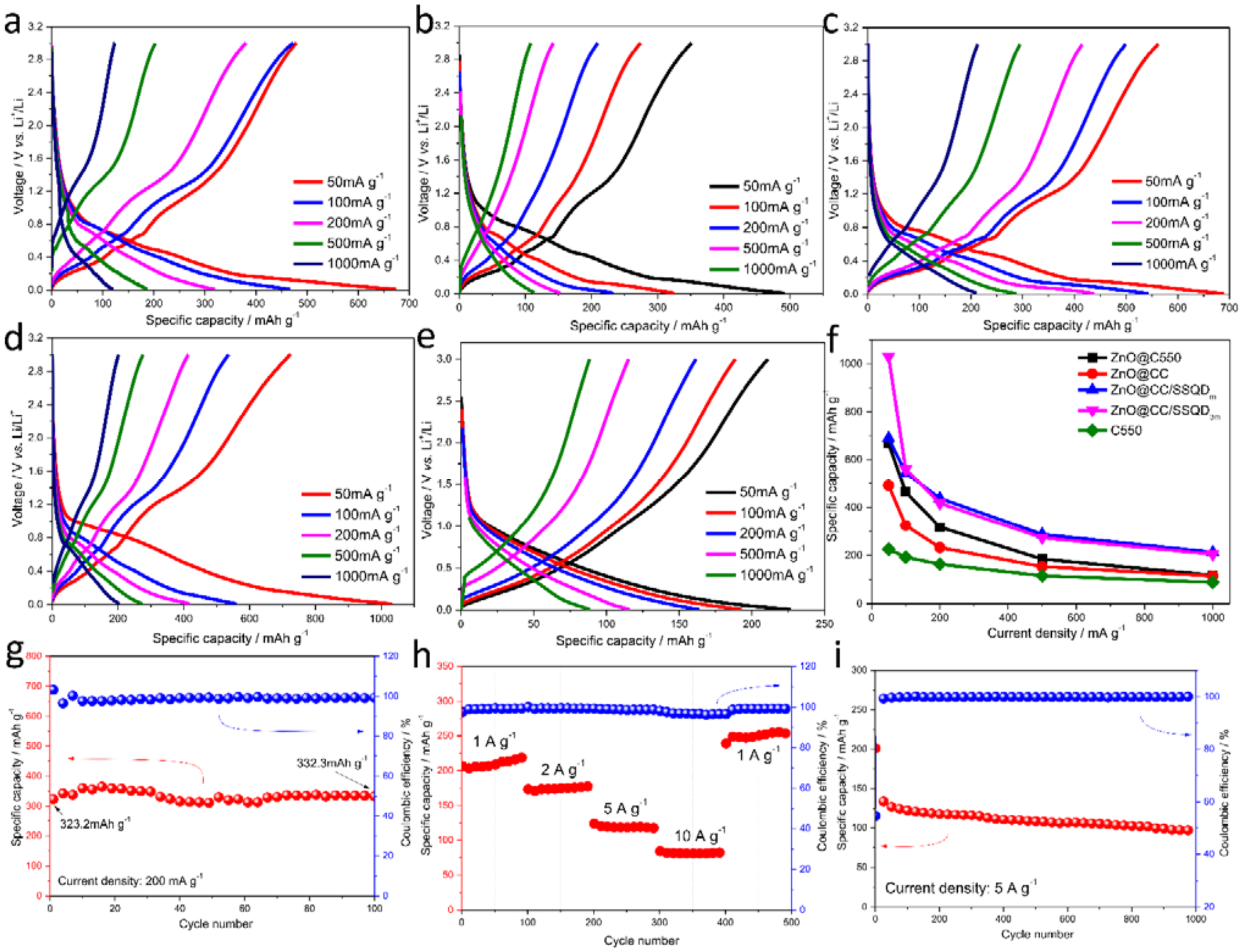

Figure 6 Galvanostatic charge/discharge properties of (a) ZnO@C550, (b) ZnO@CC, (c) ZnO@CC/SSQD$_m$, (d)ZnO@CC/SSQD$_{3m}$ and (e) C550. The capacities at different current densities are compared in (f). Rate and cycling performance of (g) ZnO@C550 at 200 mA g^{-1}, (h) ZnO@CC/SSQD$_m$ at 500-1000 mA g^{-1} and (i) ZnO@CC/SSQD$_m$ at 5 A g^{-1}.

Table 1 The specific capacity (mAh g^{-1}) of the as-prepared samples at the specific current densities.

sample	50 mA g^{-1}	100 mA g^{-1}	200 mA g^{-1}	500 mA g^{-1}	1000 mA g^{-1}
ZnO@C550	667	465	318	185	118
ZnO@CC	492	325	233	154	115
ZnO@CC/SSQD$_m$	690	544	438	288	213
ZnO@CC/SSQD$_{3m}$	1030	560	418	274	205
C550	226	193	164	116	89

Figures 6a-e display the galvanostatic charge/discharge curves of ZnO@C550, ZnO@CC, ZnO@CC/SSQD$_m$, ZnO@CC/SSQD$_{3m}$ and C550. The specific capacities at corresponding current densities are listed in Table 1 and plotted in Figure 6f. ZnO@CC has lower capacities than the parent matrix, ZnO@C550, indicating that when SSQDs are introduced into the system in a glucose solution the decomposed organic makes a negligible contribution to the increased capacity. When 1 mg SSQDs were added to 180 mg ZnO@C550 to form ZnO@CC/SSQD$_m$,, this improves both the capacity at low current density, owing to the silver nanoparticles increasing the connectivity in the matrix, and leads to a lower drop in performance with increasing current density. Further increase of the amount of SSQDs (3 mg) in the composite, ZnO@CC/SSQD$_{3m}$, results in only a limited change in the device performance at higher current densities but an enhanced capacity at low current densities, 50 and 100 mA g^{-1}. The amorphous carbon, C550 derived by treating ZnO@C550 in a strong base, has negligible capacity (see Figure S13).

At 200 mA g^{-1} as shown in Figure 6g, ZnO@C550 shows stable cycling performance in capacity and coulobmic efficiency. The device maintains a capacity of 332.3 mAh g^{-1} with an efficiency of nearly 100% after 100 cycles. At higher current density (500mA g^{-1}) the capacity of ZnO@C550 suffers fluctuations (200 mAh g^{-1} at the 500th cycle) which are ascribed to the activation of dispersed ZnO crystals, see Figure S14. ZnO@CC/SSQD$_m$ retains a capacity of 294 mAh g^{-1}after 500 cycles while ZnO@CC/SSQD$_{3m}$ only retains 136mAh g^{-1} and suffers fluctuant capacities during cycling. The *in-situ* high frequency resistance (HFR) measurement tracing the 500 cycles of ZnO@CC/SSQD$_{3m}$ displays the point resistance at 1000 and 100 HZ respectively. The up and down of the HFR correlate with the decrease and increase in capacity well, indicating the HFR of the electrode is responsible for the fluctuations in capacity during cycling. Figure 6h shows the rate performance of ZnO@CC/SSQD$_m$ at 1, 2, 5 and 10 A g^{-1} and each current has 100 cycles. The stable and average capacities are 208, 175, 118 and 81 mAh g^{-1} respectively, and after 400 cycles, the average value of 248mAh g^{-1} is recovered at 1 A g^{-1}. The long-term and high-rate cycling of ZnO@CC/SSQD$_m$ at 5A g^{-1} is shown in Figure 6i. The capacity is still 97 mAh g^{-1} after 1000 cycles with a high coulombic efficiency of 99.8%. The ZnS layer out of ZnO crystal is able to buffer the volume change during lithiation and delithiation, and the performance in lithium ion storage is comparable with the published works[30, 33, 37].

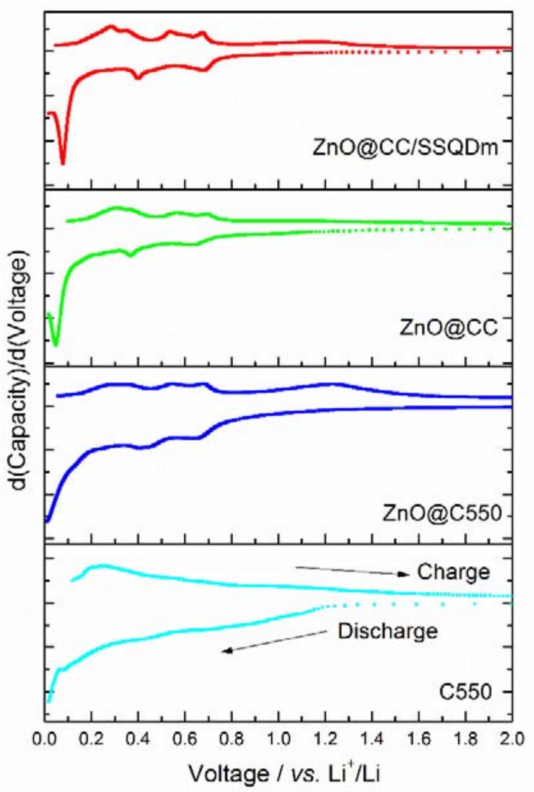

Figure 7 The dCapacity/dVoltage vs. V curve calculated from the galvanostatic charge/discharge curves at 200 mA g^{-1} of C550, ZnO@C550, ZnO@CC and ZnO@CC/SSQD$_m$.

The differential capacity, d(Capacity)/d(Voltage) against Voltage curves of C550, ZnO@C550, ZnO@CC and ZnO@CC/SSQD$_m$ at a current density of 200 mA g^{-1} are displayed in Figure 7. This representation exaggerates peaks due to charge transfer processes and makes it easier to differentiate redox processes than the CVs discussed above. The differential capacity trace for C550 shows no sharp peaks and is consistent with lithiation/delithiation of an amorphous carbon material. ZnO@C550 and ZnO@CC display five and three peaks in charge and discharge, consistent with multiple redox reactions and alloying/de-alloying steps. The features for the ZnO@CC/SSQD$_m$ are much sharper than for the other samples, pointing to improved electron transport in the matrix. In the top plot of Figure 7 the first charging peak is clearly split into two, possibly as a result of the voltage shift for the reactions of ZnS and ZnO with lithium.

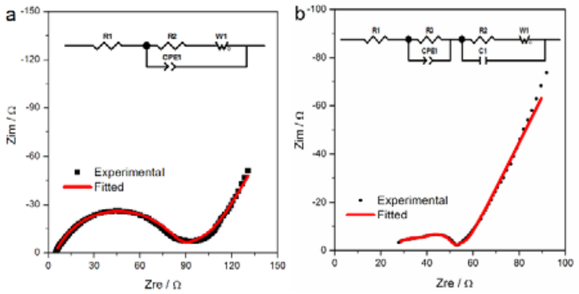

Figure 8 EIS of ZnO@CC/SSQD$_m$ and the fitted results for the (a) 12th and (b) 500th cycle. The inset shows the relevant equivalent circuit.

The impedance change of the as-prepared ZnO@CC/SSQD$_m$ anode materials with cycling was monitored using Electrochemical Impedance Spectroscopy (EIS). Figures 8(a) and (b) depict the Nyquist plots for ZnO@CC/SSQD$_m$ electrodes cycled 12 and 500 times. The equivalent circuits employed to fit the experimental data are shown as insets. In both equivalent circuits, R1 represents the purely Ohmic internal resistance of the cell that results from the electrode and electrolyte. CPE1 (constant phase element) is the pseudocapacitance of the porous electrode. R2 represents the charge transfer resistance and W1 is a Warburg component arising from the solid-state diffusion of Li ions into the bulk. Long-term cycling, 500 cycles, produces R3 in Figure 8(b), which is the surface resistance attributed to the thickening solid electrolyte interphase (SEI) film on the electrode[38-40], and C1, the capacitor in the bulk associated with Li$^+$ ions insertion. The values of the components that yielded the best fit to the experimental data are shown in Figures 8a and 8b, with values, errors listed in Table S2 and S3. For both ZnO@CC/SSQD$_m$ and ZnO@C550, shown in Figure S15-16, the charge transfer resistance, R2, is found to decrease after 500 cycles, pointing to the facile insertion/desertion reaction of lithium ions through an enhanced electrochemical interface of the electrode with cycling. The smaller R2 value for ZnO@CC/SSQD$_m$, in comparison to that of ZnO@C550, confirms the improved conductivity, indicating a conductive network of Ag nanoparticles (Scheme 1).

Conclusions

It has been demonstrated that introduction of silver sulfide nanoparticles into a carbon/nano-ZnO matrix, formed by the decomposition of distorted MOF-5, and the subsequent heat treatment of the composite significantly enhances the performance of the material as an anode in a lithium ion battery. At low current densities (200 mA g^{-1}), treatment of ZnO@C with Ag_2S QDs results in a 38% improvement in the specific capacity. High-rate and cycling performance are also improved remarkably compared with untreated samples. Characterization of the composite and analysis of its performance as an anode material points to improved connectivity and electron transport as a result of incorporation of Ag nanoparticles in the matrix and improved cyclability due to the partial sulfidation of the surface of the material. The methodology has the potential to be used with other carbon-metal oxide composites to improve their performance in energy storage applications.

ASSOCIATED CONTENT

Supporting Information. More characterization results.

AUTHOR INFORMATION

Corresponding Author

jason.riley@imperial.ac.uk (Jason Riley)

Notes

The authors declare no competing interests.

ACKNOWLEDGMENT

We thank the President's Ph.D. Scholarship of Imperial College London, the Engineering and Physical Sciences Research Council (EPSRC, Grant: EP/L015277/1) and STFC Futures Early Career Award for financial support.

REFERENCES

1. Mahmood, N.; Tang, T.; Hou, Y., Nanostructured Anode Materials for Lithium Ion Batteries: Progress, Challenge and Perspective. *Adv. Energy Mater.* **2016,** *6* (17), 1600374(1)-1600374(22).
2. Xi, K.; Cao, S.; Peng, X.; Ducati, C.; Kumar, R. V.; Cheetham, A. K., Carbon with Hierarchical Pores from Carbonized Metal-organic Frameworks for Lithium Sulphur Batteries. *Chem. Commun.* **2013,** *49* (22), 2192-2194.
3. Lu, Y.; Zhan, W.; He, Y.; Wang, Y.; Kong, X.; Kuang, Q.; Xie, Z.; Zheng, L., MOF-templated Synthesis of Porous Co_3O_4 Concave Nanocubes with High Specific Surface Area and Their Gas Sensing Properties. *ACS Appl. Mater. Interfaces* **2014,** *6* (6), 4186-4195.
4. Luz, I.; Loiudice, A.; Sun, D. T.; Queen, W. L.; Buonsanti, R., Understanding the Formation Mechanism of Metal Nanocrystal@MOF-74 Hybrids. *Chem. Mater.* **2016,** *28* (11), 3839-3849.
5. Yang, S. J.; Nam, S.; Kim, T.; Im, J. H.; Jung, H.; Kang, J. H.; Wi, S.; Park, B.; Park, C. R., Preparation and Exceptional Lithium Anodic Performance of Porous Carbon-coated ZnO Quantum Dots Derived from a Metal-organic Framework. *J. Am. Chem. Soc.* **2013,** *135* (20), 7394-7397.
6. Kim, J.; Dolgos, M. R.; Lear, B. J., Isolation and Chemical Transformations Involving a Reactive Intermediate of MOF-5. *Cryst. Growth Des.* **2015,** *15* (10), 4781-4786.
7. Huang, L.; Wang, H.; Chen, J.; Wang, Z.; Sun, J.; Zhao, D.; Yan, Y., Synthesis, Morphology Control, and Properties of Porous Metal–organic Coordination Polymers. *Microporous Mesoporous Mater.* **2003,** *58* (2), 105-114.
8. Hafizovic, J.; Bjørgen, M.; Olsbye, U.; Dietzel, P. D. C.; Bordiga, S.; Prestipino, C.; Lamberti, C.; Lillerud, K. P., The Inconsistency in Adsorption Properties and Powder XRD Data of MOF-5 Is Rationalized by Framework Interpenetration and the Presence of Organic and Inorganic Species in the Nanocavities. *J. Am. Chem. Soc.* **2007,** *129* (12), 3612-3620.
9. Lu, L.; Li, X.-Y.; Liu, X.-Q.; Wang, Z.-M.; Sun, L.-B., Enhancing the Hydrostability and Catalytic Performance of Metal-organic Frameworks by Hybridizing with Attapulgite, a Natural Clay. *J. Mater. Chem. A* **2015,** *3* (13), 6998-7005.
10. Wu, C.-M.; Rathi, M.; Ahrenkiel, S. P.; Koodali, R. T.; Wang, Z., Facile Synthesis of MOF-5 Confined in SBA-15 Hybrid Material with Enhanced Hydrostability. *Chem. Commun.* **2013,** *49* (12), 1223-1225.
11. Chen, B.; Wang, X.; Zhang, Q.; Xi, X.; Cai, J.; Qi, H.; Shi, S.; Wang, J.; Yuan, D.; Fang, M., Synthesis and Characterization of the Interpenetrated MOF-5. *J. Mater. Chem.* **2010,** *20* (18), 3758-3767.
12. Xie, Q.; Ma, Y.; Wang, X.; Zeng, D.; Wang, L.; Mai, L.; Peng, D.-L., Electrostatic Assembly of Sandwich-like Ag-C@ZnO-C@Ag-C Hybrid Hollow Microspheres with Excellent High-Rate Lithium Storage Properties. *ACS Nano* **2016,** *10* (1), 1283-1291.
13. Wang, Y.; Jiang, X.; Yang, L.; Jia, N.; Ding, Y., In Situ Synthesis of C/Cu/ZnO Porous Hybrids as Anode Materials for Lithium Ion Batteries. *ACS Appl. Mater. Interfaces* **2014,** *6* (3), 1525-1532.
14. Fu, Y.; Zhang, Z.; Yang, X.; Gan, Y.; Chen, W., ZnS Nanoparticles Embedded in Porous Carbon Matrices as Anode Materials for Lithium Ion Batteries. *RSC. Adv.* **2015,** *5* (106), 86941-86944.
15. Yan, H.; Li, T.; Lu, Y.; Cheng, J.; Peng, T.; Xu, J.; Yang, L.; Hua, X.; Liu, Y.; Luo, Y., Template-free Synthesis of Ordered ZnO@ZnS Core-shell Arrays for High Performance Supercapacitors. *Dalton Trans.* **2016,** *45* (44), 17980-17986.
16. Zheng, Y.; Zhou, T.; Zhao, X.; Pang, W. K.; Gao, H.; Li, S.; Zhou, Z.; Liu, H.; Guo, Z., Atomic Interface Engineering and Electric-Field Effect in Ultrathin Bi_2MoO_6

Nanosheets for Superior Lithium Ion Storage. *Adv. Mater.* **2017,** *29* (26), 1700396(1)-1700396(8).

17. Zheng, Y.; Zhou, T.; Zhang, C.; Mao, J.; Liu, H.; Guo, Z., Boosted Charge Transfer in SnS/SnO_2 Heterostructures: Toward High Rate Capability for Sodium-Ion Batteries. *Angew. Chem., Int. Ed.* **2016,** *55* (10), 3408-3413.

18. Zhang, Y.; Liu, Y.; Li, C.; Chen, X.; Wang, Q., Controlled Synthesis of Ag_2S Quantum Dots and Experimental Determination of the Exciton Bohr Radius. *J. Phys. Chem. C* **2014,** *118* (9), 4918-4923.

19. Zhang, Y.; Hong, G.; Zhang, Y.; Chen, G.; Li, F.; Dai, H.; Wang, Q., Ag_2S Quantum Dot: A Bright and Biocompatible Fluorescent Nanoprobe in the Second Near-Infrared Window. *ACS Nano* **2012,** *6* (5), 3695-3702.

20. Li, H.; Eddaoudi, M.; O'Keeffe, M.; Yaghi, O. M., Design and Synthesis of an Exceptionally Stable and Highly Porous Metal-organic Framework. *Nature* **1999,** *402* (6759), 276-279.

21. Yaghi, O. M.; O'Keeffe, M.; Ockwig, N. W.; Chae, H. K.; Eddaoudi, M.; Kim, J., Reticular Synthesis and the Design of New Materials. *Nature* **2003,** *423* (6941), 705-714.

22. Liu, D.; Purewal, J. J.; Yang, J.; Sudik, A.; Maurer, S.; Mueller, U.; Ni, J.; Siegel, D. J., MOF-5 Composites Exhibiting Improved Thermal Conductivity. *Int. J. Hydrogen Energy* **2012,** *37* (7), 6109-6117.

23. Liu, H.; Li, W.; Shen, D.; Zhao, D.; Wang, G., Graphitic Carbon Conformal Coating of Mesoporous TiO_2 Hollow Spheres for High-Performance Lithium Ion Battery Anodes. *J. Am. Chem. Soc.* **2015,** *137* (40), 13161-13166.

24. Cuscó, R.; Alarcón-Lladó, E.; Ibáñez, J.; Artús, L.; Jiménez, J.; Wang, B.; Callahan, M. J., Temperature Dependence of Raman Scattering in ZnO. *Phys. Rev. B* **2007,** *75* (16), 165202(1)-165202(11).

25. Zeng, Y.; Zhang, T.; Wang, L.; Wang, R.; Fu, W.; Yang, H., Synthesis and Ethanol Sensing Properties of Self-Assembled Monocrystalline ZnO Nanorod Bundles by Poly(ethylene glycol)-Assisted Hydrothermal Process. *J. Phys. Chem. C* **2009,** *113* (9), 3442-3448.

26. Lee, K. T.; Ji, X.; Rault, M.; Nazar, L. F., Simple Synthesis of Graphitic Ordered Mesoporous Carbon Materials by a Solid-state Method Using Metal Phthalocyanines. *Angew. Chem., Int. Ed.* **2009,** *48* (31), 5661-5665.

27. Gaarenstroom, S. W.; Winograd, N., Initial and final state effects in the ESCA spectra of cadmium and silver oxides. *J. Chem. Phys.* **1977,** *67* (8), 3500-3506.

28. Chen, C.; Li, Z.; Lin, H.; Wang, G.; Liao, J.; Li, M.; Lv, S.; Li, W., Enhanced Visible Light Photocatalytic Performance of ZnO Nanowires Integrated with CdS and Ag_2S. *Dalton Trans.* **2016,** *45* (9), 3750-3758.

29. Barreca, D.; Gasparotto, A.; Maragno, C.; Tondello, E.; Spalding, T. R., Analysis of Nanocrystalline ZnS Thin Films by XPS. *Surf. Sci. Spectra* **2002,** *9* (1), 54-61.

30. Ahmad, M.; Yingying, S.; Nisar, A.; Sun, H.; Shen, W.; Wei, M.; Zhu, J., Synthesis of Hierarchical Flower-like ZnO Nanostructures and Their Functionalization by Au Nanoparticles for Improved Photocatalytic and High Performance Li-ion Battery Anodes. *J. Mater. Chem.* **2011,** *21* (21), 7723-7729.

31. Liao, H.-C.; Kuo, P.-C.; Lin, C.-C.; Chen, S.-Y., Synthesis and Optical Properties of ZnO–ZnS Core-shell Nanotube Arrays. *J. Vac. Sci. Technol. B* **2006,** *24* (5), 2198-2201.

32. Shilpa; Basavaraja, B. M.; Majumder, S. B.; Sharma, A., Electrospun Hollow Glassy Carbon-reduced Graphene Oxide Nanofibers with Encapsulated ZnO Nanoparticles: a Free Standing Anode for Li-ion Batteries. *J. Mater. Chem. A* **2015,** *3* (10), 5344-5351.

33. Sun, X.; Zhou, C.; Xie, M.; Sun, H.; Hu, T.; Lu, F.; Scott, S. M.; George, S. M.; Lian, J., Synthesis of ZnO Quantum Dot/Graphene Nanocomposites by Atomic Layer Deposition with High Lithium Storage Capacity. *J. Mater. Chem. A* **2014,** *2* (20), 7319-7326.

34. Chen, C.; Wen, Y.; Hu, X.; Ji, X.; Yan, M.; Mai, L.; Hu, P.; Shan, B.; Huang, Y., Na^+ Intercalation Pseudocapacitance in Graphene-coupled Titanium Oxide Enabling Ultra-fast Sodium Storage and Long-term Cycling. *Nat. Commun.* **2015,** *6* (6929), 1-8.

35. Song, W.; Cao, X.; Wu, Z.; Chen, J.; Zhu, Y.; Hou, H.; Lan, Q.; Ji, X., Investigation of the Sodium Ion Pathway and Cathode Behavior in $Na_3V_2(PO_4)_2F_3$ Combined via a First Principles Calculation. *Langmuir* **2014,** *30* (41), 12438-12446.

36. Song, W. X.; Ji, X. B.; Wu, Z. P.; Zhu, Y. R.; Yao, Y. P.; Huangfu, K.; Chen, Q. Y.; Banks, C. E., Na_2FePO_4F Cathode Utilized in Hybrid-ion Batteries: a Mechanistic Exploration of Ion Migration and Diffusion Capability. *J. Mater. Chem. A* **2014,** *2* (8), 2571-2577.

37. Liu, J.; Li, Y.; Ding, R.; Jiang, J.; Hu, Y.; Ji, X.; Chi, Q.; Zhu, Z.; Huang, X., Carbon/ZnO Nanorod Array Electrode with Significantly Improved Lithium Storage Capability. *J. Phys. Chem. C* **2009,** *113* (20), 9008-9008.

38. Wu, Q.; Xu, J.; Yang, X.; Lu, F.; He, S.; Yang, J.; Fan, H. J.; Wu, M., Ultrathin Anatase TiO_2 Nanosheets Embedded with TiO_2-B Nanodomains for Lithium-Ion Storage: Capacity Enhancement by Phase Boundaries. *Adv. Energy Mater.* **2015,** *5* (7), 1401756(1)-1401756(9).

39. Song, W.; Chen, J.; Ji, X.; Zhang, X.; Xie, F.; Riley, D. J., Dandelion-shaped TiO_2/Multi-layer Graphene Composed of TiO_2(B) Fibrils and Anatase TiO_2 Pappi Utilizing Triphase Boundaries for Lithium Storage. *J. Mater. Chem. A* **2016,** *4* (22), 8762-8768.

40. Cheng, X.-B.; Zhang, Q., Dendrite-free Lithium Metal Anodes: Stable Solid Electrolyte Interphases for High-efficiency Batteries. *J. Mater. Chem. A* **2015,** *3* (14), 7207-7209.

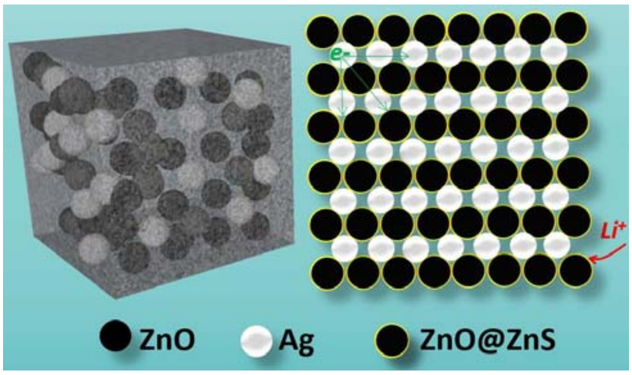
e-
Li+
ZnO
Ag
ZnO@ZnS

Supporting Information

Enhancing Distorted Metal Organic Framework Derived ZnO as Anode Material for Lithium Storage by the Addition of Ag_2S Quantum Dots

Weixin Song[a], Rowena Brugge[a], Ioannis G. Theodorou[a], Alvin Lukai Lim[b], Yuchen Yang[c], Tingting Zhao[c], Clare H. Burgess[a], Ian D. Johnson[c], Ainara Aguadero[a], Paul R. Shearing[b], Dan J.L. Brett[b], Fang Xie[a], D. Jason Riley[a]*

[a] Department of Materials, Imperial College London, London SW7 2AZ UK. Centre for Nanotechnology, London SW7 2AZ, UK.

[b] Department of Chemical Engineering, University College London, London WC1 E6BT UK.

[c] Department of Chemistry, University College London, London WC1 E6BT UK.

Corresponding Author

jason.riley@imperial.ac.uk (Jason Riley)

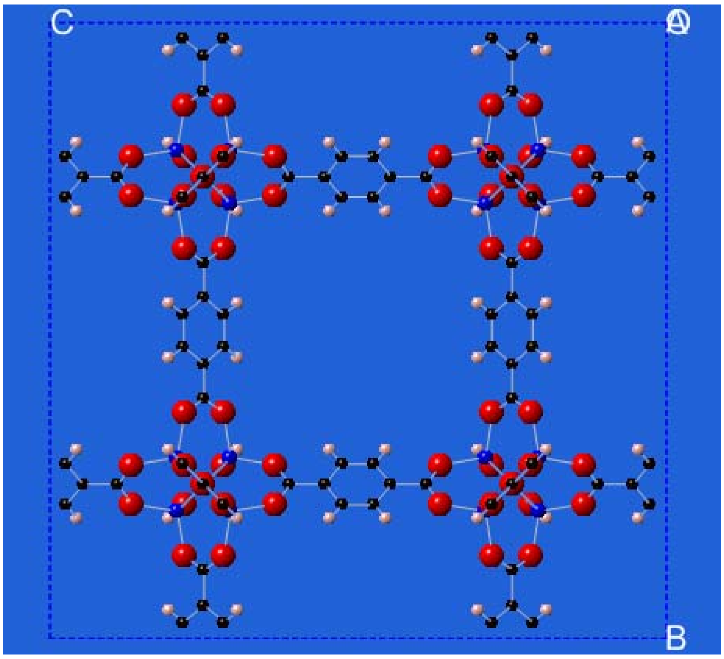

Figure S1 Structure of MOF-5. Red is oxygen, grey is hydrogen, black is carbon and blue is zinc atom.

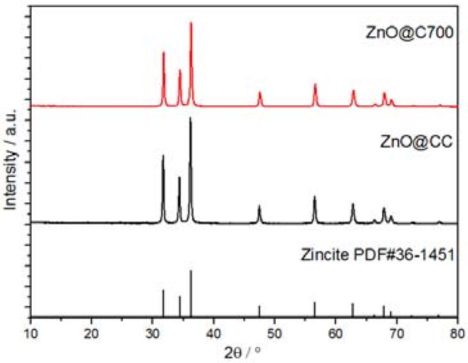

Figure S2 XRD patterns of as-prepared ZnO@C700 and ZnO@CC.

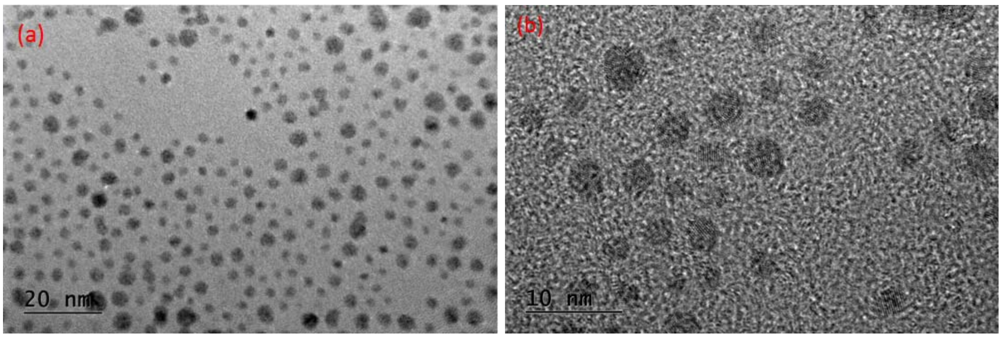

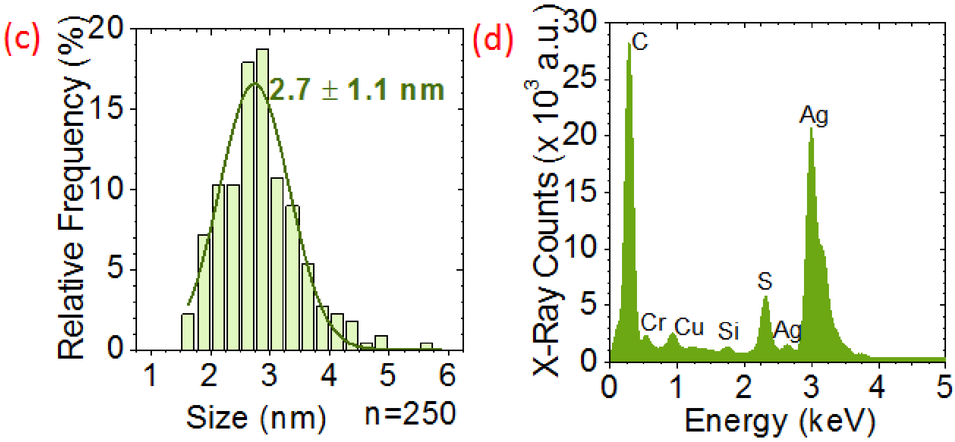

Figure S3 (a) TEM image, (b) HRTEM image, (c) Size distribution and (d) EDX of SSQD.

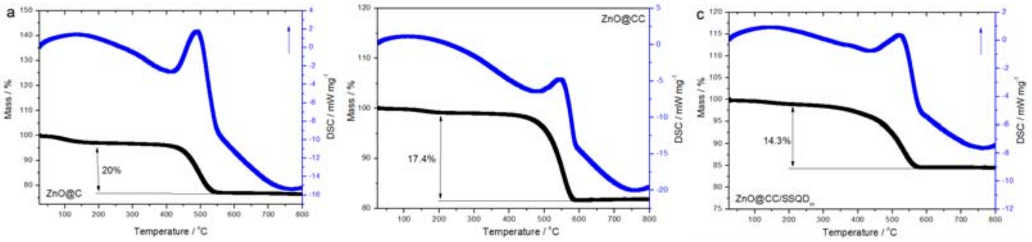

Figure S4 TGA/DSC curves of (a) ZnO@C550, (b) ZnO@CC and (c) ZnO@CC/SSQD$_m$.

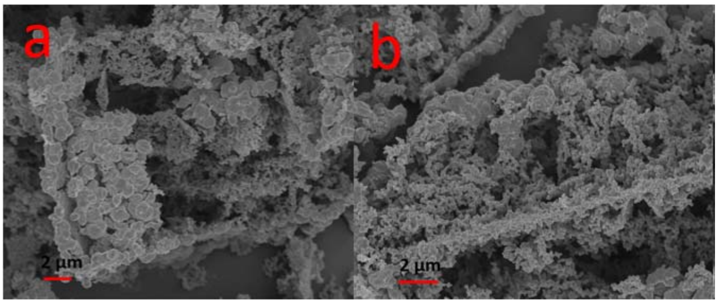

Figure S5 SEM images of ZnO@C700 from the view of (a) top and (b) cross section.

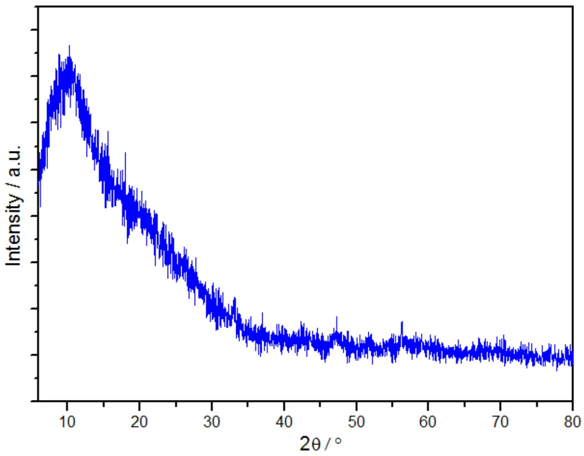

Figure S6 XRD patterns of as-prepared C550.

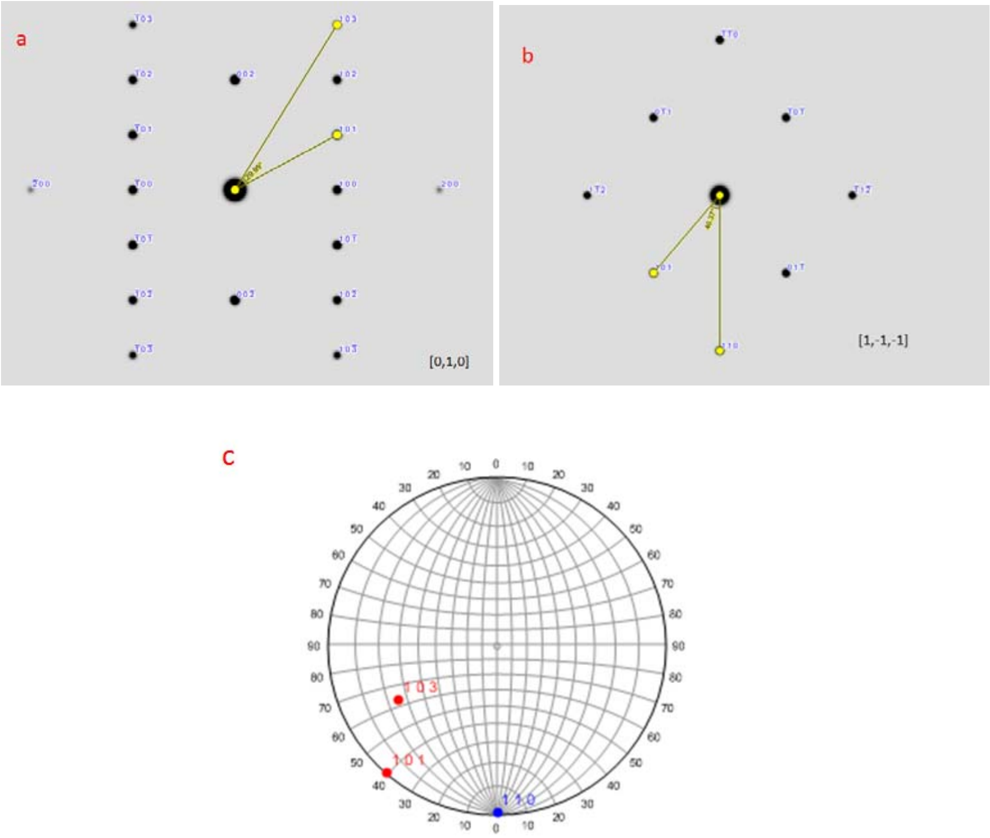

Figure S7 The angles between two lattice planes in the reciprocal space seen from (a) [010] and (b) [1,-1,-1] direction. (c) Stereographic projection to show the related reciprocal points.

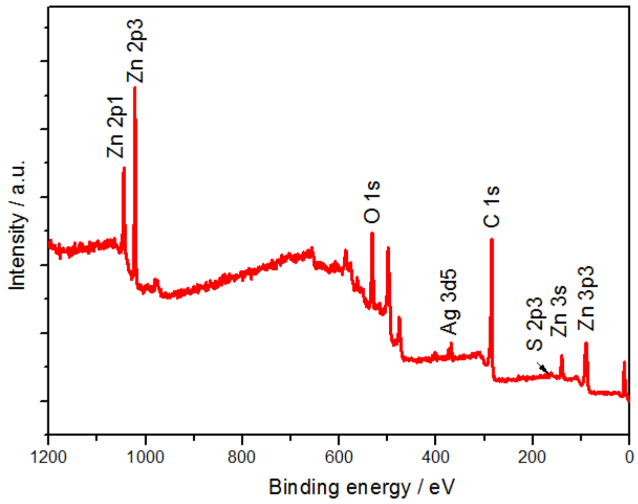

Figure S8 XPS spectrum of ZnO@CC/SSQD$_m$.

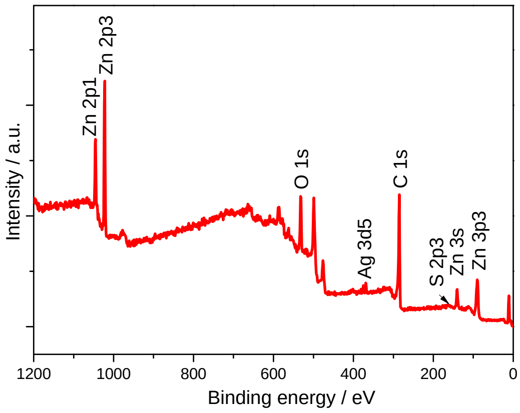

Figure S9 XPS spectrum of ZnO@CC/SSQD$_{3m}$.

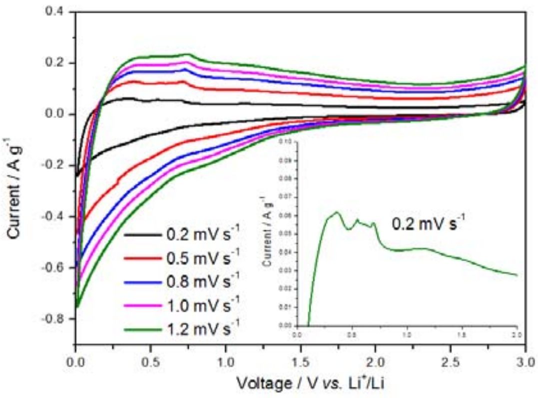

Figure S10 CV curves of ZnO@CC at different scan rates.

Table S1 The integrated area of CV peaks around 0.5 V at 0.5 mV s^{-1} of ZnO@C550, ZnO@CC, ZnO@CC/SSQD$_m$ and ZnO@CC/SSQD$_{3m}$

Phase	Area/ C g^{-1}
ZnO@C550	0.03066
ZnO@CC	0.04662
ZnO@CC/SSQD$_m$	0.1090
ZnO@CC/SSQD$_{3m}$	0.1286

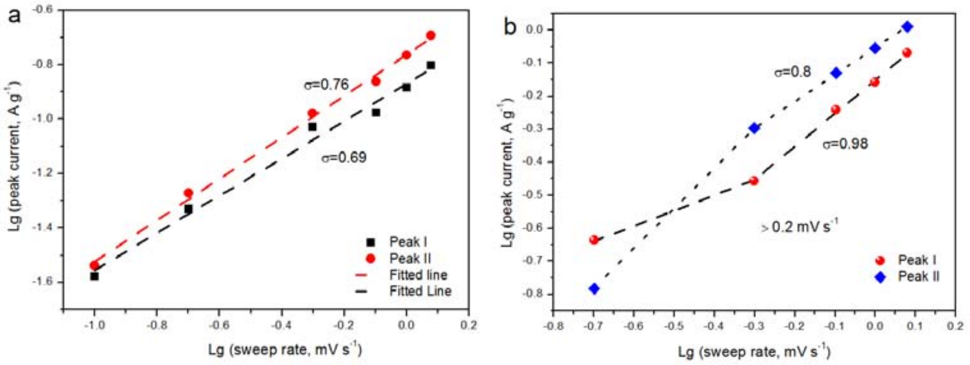

Figure S11 The relationship between log*v* and log*i* of (a) ZnO@C550 and (b) ZnO@CC/SSQD$_{3m}$.

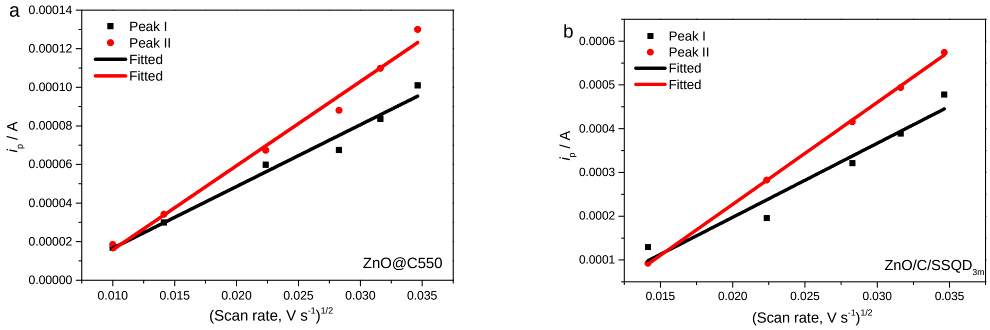

Figure S12 The linear relationship between the anodic peak current (i_p) and square root of scan rates resulting from the CV curves of (a) ZnO@C550 and (b) ZnO@CC/SSQD$_{3m}$.

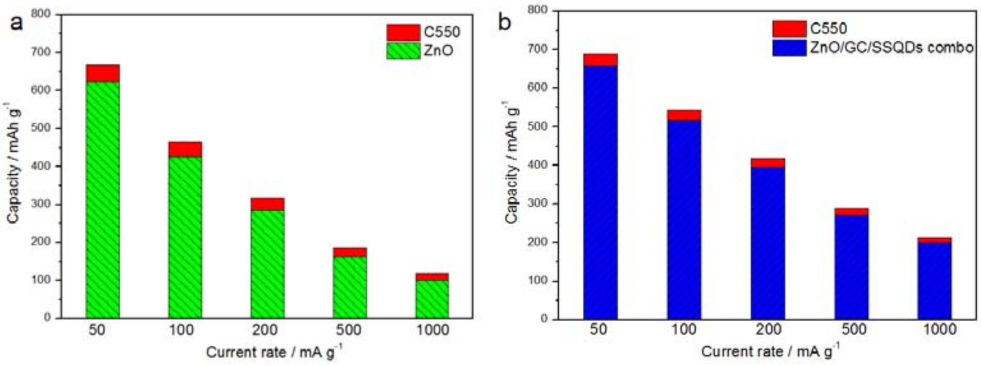

Figure S13 The capacity contribution from (a) C550 and ZnO for ZnO@C550, (b) C550 and ZnO/GC/SSQD combo for ZnO@CC/SSQD$_m$.

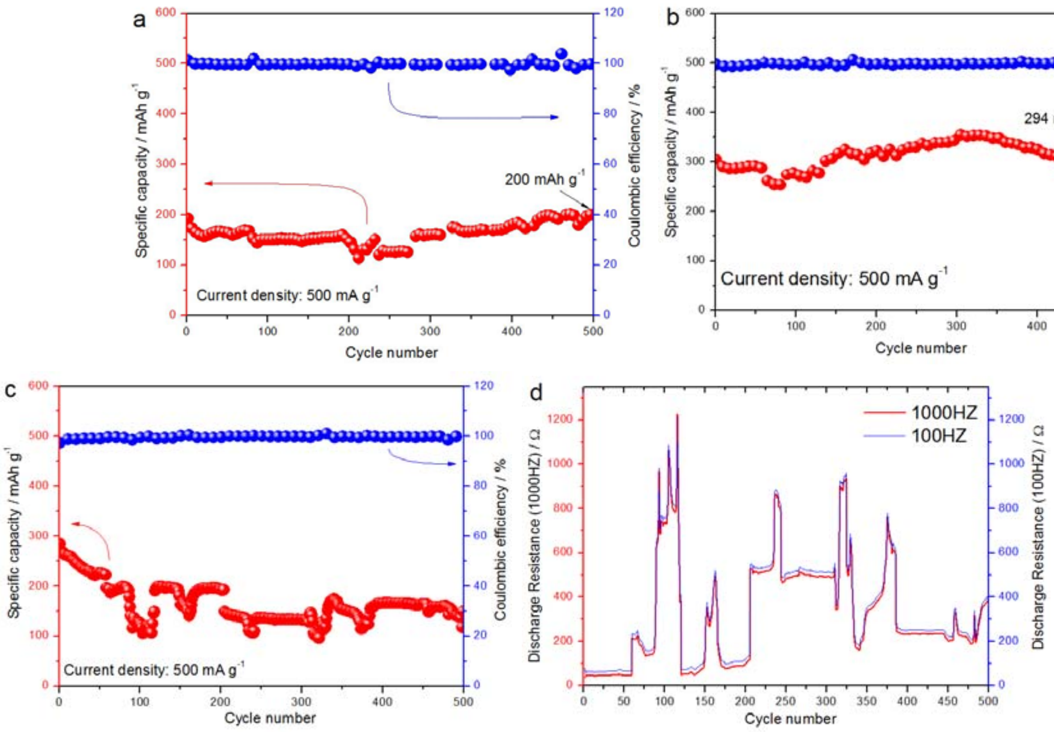

Figure S14 Cycling properties at 500 mA g^{-1}. (a) ZnO@C550, (b) ZnO@CC/SSQD$_m$ and (c) ZnO@CC/SSQD$_{3m}$. (d) High frequency resistance at 1000 and 100HZ of ZnO@CC/SSQD$_{3m}$during cycling at 500 mA g^{-1}.

Table S2 The value and error of each component in the equivalent circuit of Figure 8a. The chi-square function(χ)is 8.69×10^{-4}.

	R1/Ω	R2/Ω	CPE1/Ss^n	CPE1-P	W1/Ω	W1-T	W1-P
12-cycled	4.63	79.51	3.45E-5	0.73	60.8	13.39	0.33
Error/ %	1.66	0.95	83.83	0.55	12.36	23.04	5.78

Table S3 The value and error of each component in the equivalent circuit of Figure 8b.The chi-square function(χ) is 9.31×10^{-4}.

	R1/Ω	R2/Ω	CPE1/Ss^n	CPE1-P	W1/Ω	W1-T	W1-P	C1/F	R3/Ω
500-cycled	24.77	9.28	4.92E-5	0.65	19.55	1.77	0.35	3.56E-5	16.27
Error/ %	0.95	2.85	16.67	2.63	2.57	4.24	0.33	3.69	3.12

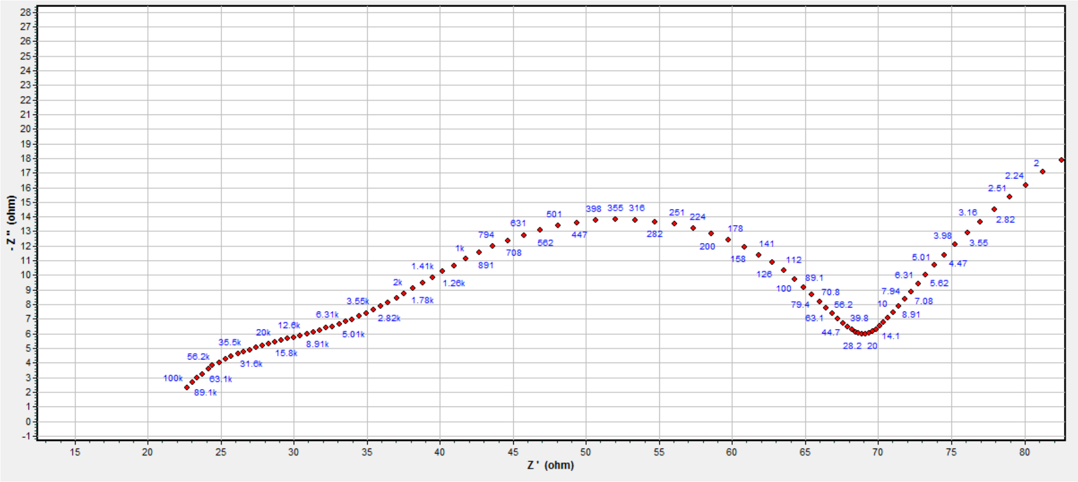

Figure S15 Nyquist plot of ZnO@CC/SSQD$_{3m}$after 500 cycles. The labeling number is the frequency.

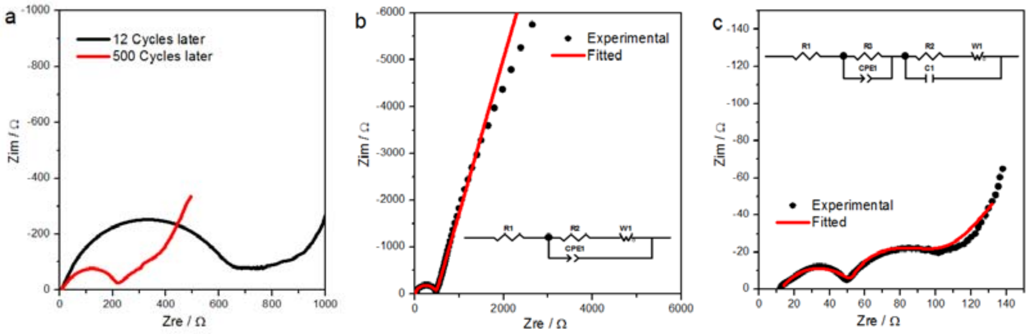

Figure S16 Nyquist plot of (a) ZnO@C550 after 12 and 500 cycles, (b) C550 after 12 cycles and (c) C550 after 500 cycles with the corresponding equivalent circuit in the inset.

Table S4 The value and error of each component in the equivalent circuit of Figure S11b.

	R1/Ω	R2/Ω	CPE1/Ss^n	CPE1-P	W1/Ω	W1-T	W1-P
12-cycled	4.83	481	6.28E-6	0.83	71967	138.6	0.81
Error/ %	4.53	1.22	5.71	0.72	4.67	6.52	0.75

Table S5 The value and error of each component in the equivalent circuit of Figure S11c.

	R1/Ω	R2/Ω	CPE1/Ss^n	CPE1-P	W1/Ω	W1-T	W1-P	C1/F	R3/Ω
500-cycled	12.57	25.83	1.6E-4	0.62	84.66	23.1	0.33	3.6E-3	41.99
Error/ %	1.85	9.16	10.1	1.94	19.84	35.69	9.39	5.62	1.65